Robust and Fast Extraction of 3D Symmetric Tensor Field Topology

Lawrence Roy, Prashant Kumar, Yue Zhang, *Member, IEEE*, and Eugene Zhang, *Senior Member, IEEE*

Fig. 1: This figure compares the quality of our degenerate curve and neutral surface extraction methods with existing work. In (a) and (b) we extract degenerate curves from a simulated cylindrical steel rod, with the bottom fixed and a tangential force applied on the top. In (a) we use the method of Palacios et al. [13], which is an adaptation of Zheng et al. [23]. In (b) we use our method. Compare the broken curves in (a) to those extracted properly using our method (b). We also compare our neutral surface extraction method in (d) with that of Palacios et al. [13] (c) for a deformation torus data set. We note that our method captures the neutral surface more completely, including the thin features in the lower-right corner. In contrast, the method of Palacios et al., based on A-patches [11], misses a significant part of the surfaces (holes in the surface in (c)). In addition to more robust extraction of these features, our methods are also faster than the respective methods of Palacios et al. [13].

Abstract—3D symmetric tensor fields appear in many science and engineering fields, and topology-driven analysis is important in many of these application domains, such as solid mechanics and fluid dynamics. Degenerate curves and neutral surfaces are important topological features in 3D symmetric tensor fields. Existing methods to extract degenerate curves and neutral surfaces often miss parts of the curves and surfaces, respectively. Moreover, these methods are computationally expensive due to the lack of knowledge of structures of degenerate curves and neutral surfaces.

In this paper, we provide theoretical analysis on the geometric and topological structures of degenerate curves and neutral surfaces of 3D linear tensor fields. These structures lead to parameterizations for degenerate curves and neutral surfaces that can not only provide more robust extraction of these features but also incur less computational cost.

We demonstrate the benefits of our approach by applying our degenerate curve and neutral surface detection techniques to solid mechanics simulation data sets.

Index Terms—Tensor field visualization, 3D symmetric tensor fields, tensor field topology, traceless tensors, degenerate curve extraction, neutral surface extraction

1 Introduction

Three-dimensional symmetric tensor fields have a wide spectrum of applications in science, engineering, and medical applications, such as solid and fluid mechanics and medical imaging. The topology of the tensor field, such as the stress and strain tensors, can provide important insights into the underlying physical phenomena.

The topology of 3D symmetric tensor fields consists of points where at least one of the eigenvector fields of the tensor field becomes discontinuous. For example, the medium eigenvector field is discontinuous at degenerate curves [22]. The *dominant eigenvector field* plays an important role in tensor field analysis. It is the major eigenvector field in linear regions (medium eigenvalue less than the average of the major and minor eigenvalues) and the minor eigenvector field in planar regions (medium eigenvalue larger than the average of the major and minor eigenvalues). The dominant eigenvector field is discontinuous at neutral surfaces [13]. These facts highlight the special roles of degenerate curves and neutral surfaces play in the topological structures in a 3D tensor field.

Despite their importance, both degenerate curves and neutral surfaces are difficult to extract. Not only are the existing methods relatively slow, they can also lead to missing parts during the extraction (Figure 1 (a) and (c)). This is due to the fact that little is understood about their geometric and topological structures. In this paper, we aim to provide analysis on degenerate curves and neutral surfaces for 3D linear tensor fields. In our analysis, the set of degenerate points in a 3D linear tensor field can be shown to be diffeomorphic to an ellipse while the set of neutral points diffeomorphic to the real projective space with a handle attached. This analysis enables more robust and faster extraction of degenerate curves and neutral surfaces in 3D symmetric fields, such as those from simulation.

The rest of the paper is organized as follows. We review related

- *Lawrence Roy is with Oregon State University. E-mail: royl@eecs.oregonstate.edu.*
- *Prashant Kumar is with Oregon State University. E-mail: kumarp@eecs.oregonstate.edu.*
- *Yue Zhang is with Oregon State University. E-mail: zhangyue@oregonstate.edu.*
- *Eugene Zhang is with Oregon State University. E-mail: zhange@eecs.oregonstate.edu.*

Manuscript received 31 Mar. 2018; accepted 1 Aug. 2018.
Date of publication 16 Aug. 2018; date of current version 21 Oct. 2018.
For information on obtaining reprints of this article, please send e-mail to: reprints@ieee.org, and reference the Digital Object Identifier below.
Digital Object Identifier no. 10.1109/TVCG.2018.2864768

work in Section 2 and relevant background on tensor fields in Section 3. We then describe our mathematical analysis and extraction method for degenerate curves in Section 4 and for neutral surfaces in Section 5, respectively. We provide performance results in Section 6. In Section 7 we show the results of applying our tensor field visualization to data sets from solid mechanics. We summarize our work in Section 8 and discuss limitations of our approaches as well as some possible future research directions.

2 Previous Work

Tensor field visualization is one of the most fundamental and well-researched topics in visualization, with applications ranging from medical imaging to fluid and solid mechanics. In this paper, we focus on topology-driven visualization techniques for 3D symmetric tensor fields and refer interested readers to recent surveys on tensor field visualization [2, 10].

Tensor field topology is first studied for 2D symmetric tensor fields by Delmarcelle and Hesselink [4], who define the notion of *degenerate points* where eigenvector fields of the tensor field have directional discontinuity. Tricoche et al. [18] provide an algorithm for the topological simplification of 2D symmetric tensor fields. Zhang et al. [19] achieve a similar goal by adapting simplification algorithms for 2D vector field topology.

Hesselink et al. [9] are the first to study degenerate points in 3D symmetric tensor fields.

There are two types of degenerate points: (a) triple (three repeating eigenvalues), and (b) double (two repeating eigenvalues). Zheng and Pang [21] point out that under structurally stable conditions, a 3D symmetric tensor field can only have double degenerate points. Moreover, these points do not live as isolated points in the space. Instead, they form curves. To extract degenerate curves, Zheng et al. [23] first identify the intersection points of degenerate curves on the faces of the mesh representing the underlying domain. These intersection points are then either directly connected to approximate the degenerate curves inside the cells of the mesh or connected through numerical integration. Tricoche et al. [17] provide an alternative approach to extracting degenerate curves. By showing that degenerate curves are a subset of ridge and valley lines of a function derived from the tensor field (the mode function), they reuse ridge and valley line extraction techniques for the extraction of degenerate curves in a tensor field. Palacios et al. [12] develop a design system for 3D symmetric tensor fields, with applications in texture and geometry synthesis. At the core of their system is the ability to deform, remove, and reconnect degenerate curves. Linear tensor fields are the simplest tensor fields, whose behaviors can be used to describe non-linear tensor fields near a point of interest, i.e., local linearization. Zhang et al. [20] study the topology of 3D linear tensor fields and provide a number of observations that are inspirational to this research. Zobel and Scheuermann [24] introduce the notion of extreme curves and surfaces for 3D symmetric tensor fields. Degenerate curves are part of extreme curves.

Palacios et al. [13] introduce the notion of neutral surfaces and point out their topological significance. They also provide a method to extract neutral surfaces based on the A-patches technique [11]. In addition, they adapt the degenerate curve extraction method of Zheng et al. [23] from hexahedral meshes to tetrahedral meshes. Furthermore, they use the A-patches technique to locate degenerate points on the faces of the mesh, which can handle cases where there are multiple degenerate points on a face.

In our paper, we provide analysis on the topological structure of the set of degenerate points and the set of neutral points in a 3D linear tensor field. Such structural analysis in turn leads to a parameterization for both degenerate curves and neutral surfaces, which enable more robust and faster extraction algorithms for 3D piece-wise linear tensor fields, such as the stress and strain tensor fields from solid mechanics simulation.

3 Tensor Background

In this section we briefly review relevant background on 3×3 symmetric tensors and tensor fields.

Let $\mathbb{K}$ be the set of 3×3 tensors, which is a nine-dimensional linear space. The trace of a tensor $T = (T_{ij})$ is $T_{11} + T_{22} + T_{33}$. For reasons to be made clear soon, we will equip an inner product in $\mathbb{K}$ as follows: given two 3×3 tensors $R = (R_{ij})$ and $S = (S_{ij})$, their inner product [15] is defined to be

$$\langle R, S \rangle = \sum_{i=1}^{3} \sum_{j=1}^{3} R_{ij} S_{ij} = \text{trace}(S^T R) \tag{1}$$

A tensor is symmetric if it equals its transpose. Given our focus in the paper, we will omit *symmetric* when referring to symmetric tensors.

A 3×3 tensor T has three *real* eigenvalues $\lambda_1 \geq \lambda_2 \geq \lambda_3$, referred to as the *major eigenvalue*, *medium eigenvalue*, and *minor eigenvalue*, respectively. When the eigenvalues are mutually distinct, T is *non-degenerate*. In this case, it is possible to choose three unit eigenvectors $\{v_1, v_2, v_3\}$ such that v_i corresponds to λ_i for any $1 \leq i \leq 3$ and v_i's form a right-hand orthonormal basis of the space. The trace of T can also be expressed as $\lambda_1 + \lambda_2 + \lambda_3$.

A tensor T can be uniquely decomposed as $\frac{trace(T)}{3}\mathbb{I} + A$ where $\mathbb{I}$ is the three-dimensional identity matrix and $A = T - \frac{trace(T)}{3}\mathbb{I}$ is the *deviator* of T. A is a *traceless* tensor, i.e., $trace(A) = 0$. More importantly, the directional information (eigenvectors) in T is contained purely in its deviator in the following sense: a vector v is an eigenvector of T if and only if v is an eigenvector of A. In fact, as we will discuss later, the *topology* of a tensor field can be defined in terms of its deviator tensor field. Another nice property of the set of traceless tensors is that it is closed under matrix addition and scalar multiplication, making it a five-dimensional linear subspace of the set of tensors. We refer to this space as $\mathbb{A}$. For the remainder of our paper, we will focus on traceless tensors and therefore omit *traceless*.

A tensor T is referred to as being *degenerate* if it has repeating eigenvalues. A (traceless) degenerate tensor T has the form $T = k(vv^T - \frac{\mathbb{I}}{3})$ for some $k \in \mathbb{R}$ and some unit vector v. T is either triple degenerate (all three eigenvalues are identical or equivalently $k = 0$) or double degenerate (two eigenvalues are the same or equivalently $k \neq 0$). For a double degenerate tensor, the eigenvalue that is distinct from the repeating eigenvalues is referred to as the *dominant eigenvalue*. When $k > 0$, the dominant eigenvalue is the major eigenvalue, and T is referred to as being a *linear degenerate tensor*. When $k < 0$, the dominant eigenvalue is the minor eigenvalue, and T is referred to as being a *planar degenerate tensor*. The set of eigenvectors corresponding to the dominant eigenvalue and the repeating eigenvalues are referred to as *dominant eigenvectors* and *repeating eigenvectors*, respectively. For a double degenerate tensor, the set of repeating eigenvectors form a plane (*repeating plane*) whose normal is a dominant eigenvector.

A tensor T is referred to as being *neutral* if its medium eigenvalue is the average of its major eigenvalue and minor eigenvalue. A (traceless) neutral tensor has the form $t = k(v_1 v_1^T - v_3 v_3^T)$ for some $k \in \mathbb{R}$ and unit vectors $v_1 \perp v_3$. While a triple degenerate tensor is also neutral, it is not structurally stable. Instead, we consider neutral tensors that have three distinct eigenvalues $|k|$, 0, $-|k|$.

The set of (traceless) degenerate tensors, referred to as $\mathbb{D}$, is a non-linear subset of $\mathbb{A}$. Similarly, the set of (traceless) neutral tensors, referred to as $\mathbb{N}$, is also a non-linear subset of $\mathbb{A}$.

A *tensor field* $T(\mathbf{p})$ is a continuous *tensor-valued* function in $\mathbb{R}^3$. A point $\mathbf{p}$ is a *(linear, planar, triple) degenerate point* if $T(\mathbf{p})$ is a degenerate tensor of a corresponding type. Given a generic tensor field, the set of triple degenerate points is structurally unstable, i.e., the structure does not persist under any arbitrarily small perturbation [3]. On the other hand, linear and planar degenerate points are structurally stable, and they form curves. Existing degenerate points extraction methods [13, 17, 21] have focused on double degenerate points, which is a goal that we follow in this work as well. Similarly, a point $\mathbf{p}$ is a *neutral* point if $T(\mathbf{p})$ is a neutral tensor. Under structurally stable conditions, the set of neutral points form surfaces [13].

4 Degenerate Curve Extraction

4.1 3D Linear Tensor Fields

In this paper we focus on the extraction of degenerate curves and neutral surfaces from a 3D tensor field defined on the vertices of a tetrahedral mesh, i.e. piecewise linear tensor fields. Such data is common in simulation. In addition, when studying the behavior of a tensor field near a point of interest, the first term of the Taylor's expansion leads to a locally linear tensor field.

A linear traceless tensor field has the form of $T(x,y,z) = T_0 + xT_x + yT_y + zT_z$ where T_0, T_x, T_y, and T_z are 3×3 traceless tensors. Let U be the image of T, i.e. the set of all tensors that occur in the field.

Under structurally stable conditions, T_0, T_x, T_y, T_z span a four-dimensional linear subspace of the five-dimensional space of traceless tensors, $\mathbb{A}$. Consequently, there exists a traceless tensor $\overline{T} \in \mathbb{A}$ which is perpendicular to T_0, T_x, T_y, and T_z based on the aforementioned inner product (Equation 1). Additionally, we normalize $\overline{T}$ so that $\langle \overline{T}, \overline{T} \rangle = 1$. Note that $\overline{T}$ plays an important role in our parameterizations of the degenerate curves and neutral surfaces of the tensor field $T(x,y,z) = T_0 + xT_x + yT_y + zT_z$. Therefore, we refer to $\overline{T}$ as the *normal* of the tensor field $T(x,y,z)$.

The tensor field, together with its normal, spans $\mathbb{A}$. As a result, we define the invertible linear map $\mathfrak{T} : \mathbb{R}^5 \to \mathbb{A}$ given by

$$\mathfrak{T}(x,y,z,w,u) = xT_x + yT_y + zT_z + wT_0 + u\overline{T} \tag{2}$$

We call its inverse $\mathfrak{T}^{-1} : \mathbb{A} \to \mathbb{R}^5$. A tensor T can occur at location (x,y,z) in the field if and only if $\mathfrak{T}^{-1}(T) = (x,y,z,1,0)$. Consequently, the process of finding degenerate curves is about finding degenerate tensors for which $\mathfrak{T}^{-1}(T)$ gives $w = 1$ and $u = 0$.

Since $\overline{T}$ is the normal of the tensor field, it can be used to find the u coordinate of $\mathfrak{T}^{-1}(T)$.

$$\begin{aligned}
&\langle \overline{T}, \mathfrak{T}(x,y,z,w,u) \rangle \\
&= \langle \overline{T}, xT_x + yT_y + zT_z + wT_0 + u\overline{T} \rangle && (3)\\
&= x\langle \overline{T}, T_x \rangle + y\langle \overline{T}, T_y \rangle + z\langle \overline{T}, T_z \rangle + w\langle \overline{T}, T_0 \rangle + u\langle \overline{T}, \overline{T} \rangle && (4)\\
&= u && (5)
\end{aligned}$$

Since $\mathfrak{T}^{-1}$ is a linear map, its other coordinates may also be written in terms of the inner product $\langle \cdot, \cdot \rangle$. Let

$$\mathfrak{T}^{-1}(T) = \big(\langle T'_x, T\rangle, \langle T'_y, T\rangle, \langle T'_z, T\rangle, \langle T'_0, T\rangle, \langle \overline{T}, T\rangle\big) \tag{6}$$

for some T'_x, T'_y, T'_z, T'_0 in $\mathbb{A}$.

From classical linear algebra results on inverse maps [15], we have that T'_0 is orthogonal to T_x, T_y, T_z, and $\overline{T}$, and has a dot product 1 with T_0. In fact, it is the unique tensor satisfying these properties. A similar implication holds for T'_x, T'_y, and T'_z.

The existence of the inverse map $\mathfrak{T}^{-1}$ leads to an important property.

Proposition 1. *Given a linear 3D tensor field $T(x,y,z) = T_0 + xT_x + yT_y + zT_z$, any tensor value can occur at most once in the domain. Moreover, if a tensor value appears in the domain, its multiples cannot occur anymore in the field.*

The proofs of the Proposition and other theoretical results can be found in the appendix (supplementary material).

In the remainder of this section, we describe our analysis of degenerate curves of a 3D linear tensor field and an efficient algorithm to extract degenerate curves from a piecewise linear tensor field using this analysis. Our discussion on neutral surfaces will be presented in Section 5.

4.2 Degenerate Point Parameterization

We start this section by providing the sufficient and necessary conditions for which a degenerate tensor can occur in a linear tensor field.

Theorem 2. *Let t be a degenerate tensor that occurs in a linear tensor field $T(x,y,z) = T_0 + xT_x + yT_y + zT_z$, and v be its dominant eigenvector. Then $v^T \overline{T} v = 0$.*

The reverse of the above theorem is true, too, as stated in the next theorem.

Theorem 3. *Given a linear tensor field $T(x,y,z) = T_0 + xT_x + yT_y + zT_z$ and a unit vector v that satisfies $v^T \overline{T} v = 0$, there exist $x_0, y_0, z_0 \in \mathbb{R}$ such that $T(x_0,y_0,z_0)$ is a degenerate tensor and v is a dominant eigenvector of $T(x_0,y_0,z_0)$. The dominant eigenvalue is given by $k = \frac{1}{v^T T'_0 v}$.*

It is useful to be able to explicitly calculate x, y, and z, given the dominant eigenvector v. Since $\mathfrak{T}^{-1}(t) = (x,y,z,1,0)$, by a similar calculation we have

$$x = kv^T T'_x v = \frac{v^T T'_x v}{v^T T'_0 v} \tag{7}$$

$$y = kv^T T'_y v = \frac{v^T T'_y v}{v^T T'_0 v} \tag{8}$$

$$z = kv^T T'_z v = \frac{v^T T'_z v}{v^T T'_0 v} \tag{9}$$

We can choose a new basis under which $\overline{T} = \begin{pmatrix} a & 0 & 0 \\ 0 & b & 0 \\ 0 & 0 & -a-b \end{pmatrix}$ where $a \geq b \geq 0$. Note that if the eigenvalues of $\overline{T}$ has two negative eigenvalues, we can simply choose $-\overline{T}$ which is still perpendicular to T_0, T_x, T_y, and T_z and has two positive eigenvalues. Also, changing the basis in the XYZ space does not alter the degenerate curves in the field.

Now the set of degenerate points in the tensor field $T(x,y,z)$ must satisfy the following equations:

$$a\alpha^2 + b\beta^2 = (a+b)\gamma^2 \tag{10}$$

$$\alpha^2 + \beta^2 + \gamma^2 = 1 \tag{11}$$

where $v = (\alpha, \beta, \gamma)$ is a unit dominant eigenvector of the degenerate tensor. Note that if (α,β,γ) satisfies the above system of equations, so does $(-\alpha,-\beta,-\gamma)$.

Recall that a traceless degenerate tensor with the unit dominant eigenvector (α,β,γ) has the form $k\begin{pmatrix} \alpha^2 - \frac{1}{3} & \alpha\beta & \alpha\gamma \\ \alpha\beta & \beta^2 - \frac{1}{3} & \beta\gamma \\ \alpha\gamma & \beta\gamma & \gamma^2 - \frac{1}{3} \end{pmatrix}$ for some $k \in \mathbb{R}$. Proposition 1 shows that any pair of solutions to Equations 10 and 11 can correspond to exactly one point in the original XYZ domain. Consequently, $\mathfrak{T}$ (from Equation 2) introduces a 2-to-1 map between the solutions to Equations 10 and 11 and the set of degenerate points in the field.

The solutions of Equations 10 and 11 can be visualized as a curve on the unit sphere in the space of α, β, and γ (Figure 2). In this figure, the degenerate curves are shown in the left of each subfigure, where green indicates linear degenerate curves while yellow indicates planar degenerate curves. In the right of each subfigure, we show a visualization of the dominant eigenvector directions, which usually form two loops with inversive symmetry. Every degenerate point in the tensor field (left of each subfigure) corresponds to two antipodal points on the curves (right of each subfigure). Starting from the upper-left subfigure and travelling clockwise, we show six degenerate points in the tensor field. For each selected degenerate point (left), we show the repeating plane whose normal is highlighted by a black dot on the loops in the corresponding right subfigure. Note that if two degenerate curves approach ∞ in opposite directions, the dominant eigenvectors approach the same limit vector. In the right subfigures, such limit vectors are the boundary between linear degenerate points (green) and planar degenerate points (yellow).

Notice that scaling (α,β,γ) does not affect Equation 10. Keeping this in mind, we may absorb Equation 11 and rescale (α,β,γ) to replace it with $\gamma = 1$. Then Equation 10 simplifies to

$$a\alpha^2 + b\beta^2 = (a+b) \tag{12}$$

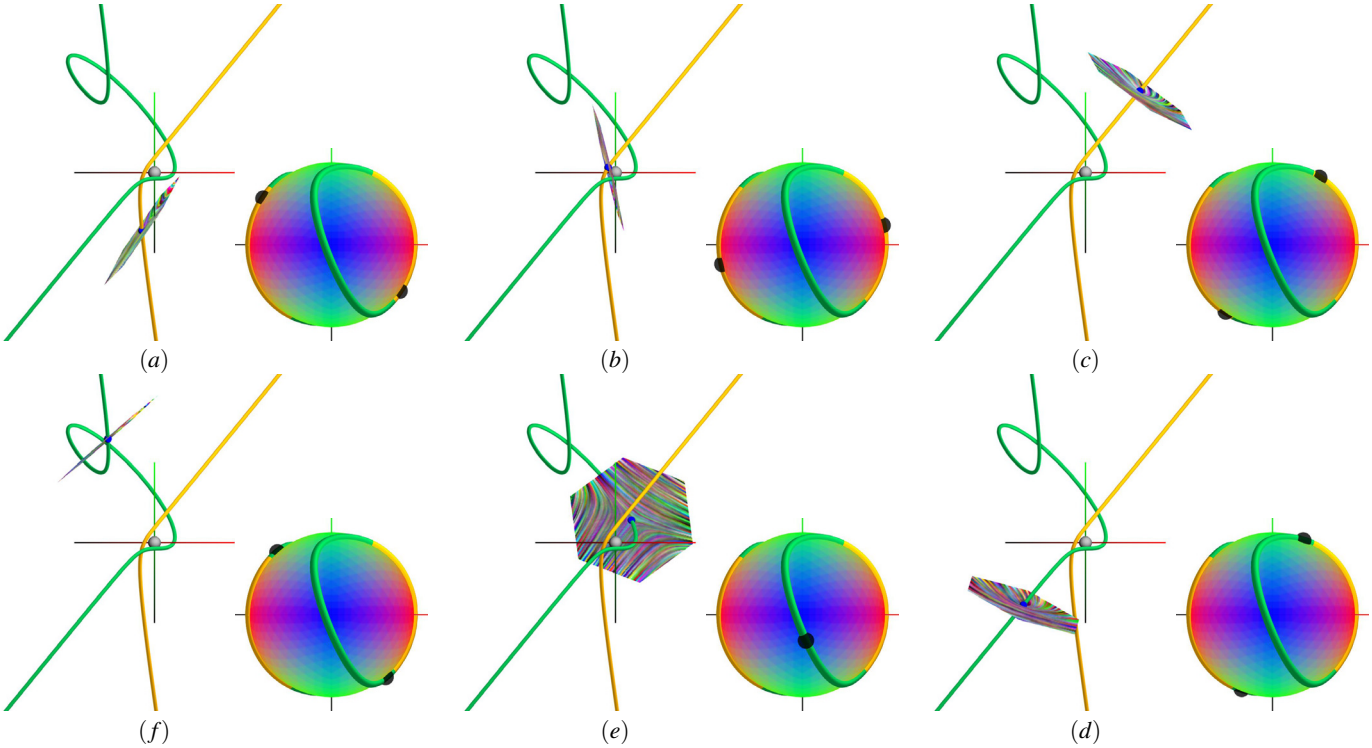

Fig. 2: This figure uses an example to show that under structurally stable conditions, there is a bijective map between the set of unit dominant eigenvectors and the degenerate points in the field. Starting from the upper-left figure and travelling clockwise, we show six degenerate points and their corresponding dominant eigenvectors (black dots on the elliptical curves surrounding the sphere). Planar degenerate points form yellow curves while linear degenerate points form green curves.

This is the equation of an ellipse, centered at the origin of the $\alpha\beta$ plane. Geometrically, this means that the projection of the curve in Figure 2 onto a plane perpendicular to $\overline{T}$'s minor eigenvector is an ellipse. We parameterize this ellipse using the angle $\theta = \text{atan2}(\beta, \alpha)$. Increasing θ will travel counterclockwise around the ellipse (Figure 2).

It is also important to know the tangent vector of the degenerate curve. We calculate this by taking the derivative of the parameterization. First, we find the tangent vector $\frac{dv}{d\theta} = (\frac{d\alpha}{d\theta}, \frac{d\beta}{d\theta}, \frac{d\gamma}{d\theta})$ of the ellipse on the sphere, to tell which way the dominant eigenvector will change as we follow the curve. From the parameterization, $\frac{dv}{d\theta}$ is continuous and nonzero. This tangent vector can then be turned into the change in the x coordinate by differentiating Equation 7.

$$\frac{dx}{d\theta} = \frac{d}{d\theta}\frac{v^T T_x' v}{v^T T_0' v} \tag{13}$$

$$= 2\frac{v^T T_x' \frac{dv}{d\theta}}{v^T T_0' v} - 2\frac{v^T T_x' v \; v^T T_0' \frac{dv}{d\theta}}{(v^T T_0' v)^2} \tag{14}$$

Similarly, for y and z we have

$$\frac{dy}{d\theta} = 2\frac{v^T T_y' \frac{dv}{d\theta}}{v^T T_0' v} - 2\frac{v^T T_y' v \; v^T T_0' \frac{dv}{d\theta}}{(v^T T_0' v)^2} \tag{15}$$

$$\frac{dz}{d\theta} = 2\frac{v^T T_z' \frac{dv}{d\theta}}{v^T T_0' v} - 2\frac{v^T T_z' v \; v^T T_0' \frac{dv}{d\theta}}{(v^T T_0' v)^2} \tag{16}$$

These derivatives are continuous when $v^T T_0' v \neq 0$, i.e. when the degenerate point is not at infinity.

4.3 Degenerate Curve Extraction Algorithm

The aforementioned parameterization of the degenerate points in a 3D linear tensor field brings a number of benefits.

First, it is now possible to extract the set of degenerate points at any given accuracy, by simply sampling the loop at sufficient resolutions. This overcomes numerical issues associated with numerical integration and finding a solution to a high-degree polynomial, both of which are essential steps in existing degenerate curve extraction methods such as [13, 17, 22]. See Figure 1 for a comparison. In this case, the degenerate point extraction method of Palacios et al. [13] in Figure 1(a) leads to broken degenerate curves and spurious degenerate points due to numerical issues. Our approach, with the knowledge of the geometric and topological structure of 3D linear tensor fields, does not suffer from this (Figure 1(b)).

Second, by avoiding the expensive, sequential computation of Runge-Kutta tracing and correction, the performance is greatly enhanced.

We now describe our algorithm for the input data, which comes in the form of a tensor field defined over a tetrahedral mesh with a piecewise linear interpolation.

Our method first extracts degenerate points on the faces in the mesh. As a preprocessing step, we follow [13] and use the A-patches method without subdivision [11] to quickly eliminate faces that have no degenerate points (We provide a review of the A-patches method in Section 5). Given a face f between two tetrahedra c_1 and c_2, consider the plane P that contains f. Note that the linear tensor fields $T_1(x,y,z)$ inside c_1 and $T_2(x,y,z)$ inside c_2 agree on P. Consequently, in the local coordinate system of P the tensor field on P has the form $T_{0,P} + rT_{r,P} + sT_{s,P}$ where r and s are the local coordinates. Under structurally stable conditions, $T_{0,P}$, $T_{r,P}$, and $T_{s,P}$ span a three-dimensional linear subspace of $\mathbb{A}$ (co-dimension two). Moreover, recall that $\mathbb{A}$ has an inner product defined on it (Section 3). Therefore, there exist two 3×3 traceless tensors $\overline{T_1}$ and $\overline{T_2}$ such that they are both perpendicular to $T_{0,P}$, $T_{r,P}$, and $T_{s,P}$. Moreover, $\overline{T_1}$ is perpendicular to $\overline{T_2}$. Note that $\overline{T_1}$ and $\overline{T_2}$ can be computed from $T_{0,P}$, $T_{r,P}$ and $T_{s,P}$ with algorithms to compute the basis for the orthogonal complement subspace [16].

If tensor $t = T_{0,P} + rT_{r,P} + sT_{s,P}$, then $v^T \overline{T_1} v = 0$ and $v^T \overline{T_2} v = 0$ where v is a unit dominant eigenvector of t (Theorem 2). This leads to

the following system of quadratic equations:

$$v^T \overline{T_1} v = 0 \quad (17)$$
$$v^T \overline{T_2} v = 0 \quad (18)$$
$$v^T v = 1 \quad (19)$$

Similar to Equation 10, Equations 17 and 18 do not depend on the length of v, so we may absorb Equation 19 and normalize v at the end. Equations 17 and 18 are then two conic sections, and we need to find their intersections. By Bézout's theorem [6], there are at most four real-valued intersection points of the two conics. Note that this could be implemented by solving a quartic. Instead, we use the method in [14] (Section 11.4) that converts the problem to finding a linear combination of $\overline{T_1}$ and $\overline{T_2}$ that is singular, for which we use the solver in Eigen [8].

Given a solution v_0 to Equations 17, 18, and 19, we construct the family of tensors $k(v_0^T v_0 - \mathbb{I})$ and look for k_0 such that $k_0(v_0^T v_0 - \mathbb{I}) = T_{0,P} + rT_{r,P} + sT_{s,P}$. This is again solved by finding the basis for complement subspace [16].

Note that if v_0 is a solution, so is $-v_0$ since both give rise to the same degenerate tensor. Therefore, inside any face of the mesh, there are at most four degenerate points. Finally, we use the barycentric coordinates of the degenerate points, i.e., (r_i, s_i), to decide which degenerate points are inside the face f (not just in the plane containing f). Only those solutions are valid solutions.

Once degenerate points inside all faces have been detected, we process each tetrahedron c as follows. First, we collect all the degenerate points at any face of c (Figure 3 (left)) and compute the corresponding points on the elliptical curve (Figure 3 (right)). Next, for each of these points we calculate whether going counterclockwise around the ellipse will enter or exit the tetrahedron, by finding the curve tangent calculated in Section 4.2 and taking the dot product with the face normal. Going counterclockwise from each entrance point to the next exit point will give those segments of the degenerate curve that are inside the tetrahedron. These sections on the loop are then sampled using the parameterization of the ellipse. The samples are placed uniformly in the parameter $\theta \in [0, 2\pi)$ at intervals of $\frac{2\pi}{1000}$, which implies that a tetrahedron covering almost the whole ellipse receives 1000 samples. Tetrahedra that cover a smaller portion of the ellipse receive fewer samples.

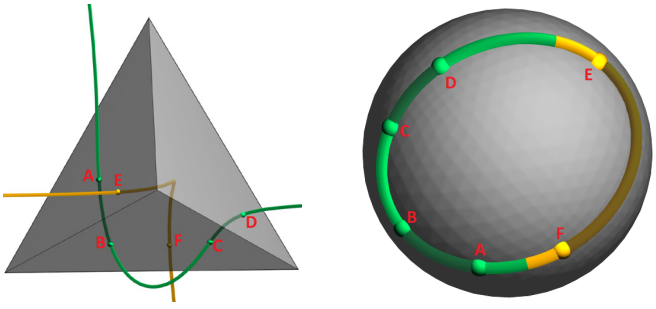

(a) (b)

Fig. 3: Illustration of the degenerate curve extraction algorithm. The darker curve segments on the sphere (b) correspond to degenerate curve segments inside the tetrahedron (a).

It is worth noting that the parameterization is not uniform, as it maps a closed curve to an infinite space. However, the derivation of the tangent vector in Section 4.2 shows that it, for the most part, cannot change too rapidly from one sample to the next. Excluding structurally unstable cases, there may be long sections of degenerate curve in $\mathbb{R}^3$ with very few points on them, but they are where the degenerate curve is almost a straight line and does not need many samples (see Figure 2 (c-d) for an example). Also, given that the input data is in a finite region, those points with the worst distortion are outside the tet.

The main numerical challenge is the presence of structurally unstable cases, such as tetrahedra for which T_0, T_x, T_y, T_z are linearly dependent, and degenerate curves intersecting the vertices and edges of the mesh. To avoid these issues we add a small amount of noise ($\sim 10^{-11}$ times the magnitude of the original tensor) to the input data. This is sufficient to avoid such cases in practice.

Note that this process is highly parallelizable, of which we take advantage to speed up the computation.

5 Neutral Surface Extraction

Neutral surfaces are another important feature in a 3D tensor field. Existing methods such as the Marching Tetrahedron method, while fast, often has topological errors during the extraction [13]. Making the observation that the neutral surface in a 3D linear tensor field is a level set of a cubic polynomial (thus an algebraic surface), Palacios et al. [13] adapt the A-patches method [11], which is a well-known technique in extracting algebraic curves and surfaces by the CAGD community. While the A-patches method is more robust than the Marching Tetrahedron method, it requires iterative mesh subdivision and does not guarantee the process will eventually terminate. Therefore, this method can still miss a significant part of the surface. In addition, the data structure needed by the A-patches method incur high memory and computational cost. Similar to degenerate curve extraction, we aim to find a parameterization for neutral surfaces. In this section, we describe such a parameterization, based on our novel tensor field analysis.

5.1 Neutral Point Parameterization

We will again consider a linear tensor field $T(x,y,z) = T_0 + xT_x + yT_y + zT_z$. Under structurally stable conditions, T_0, T_x, T_y, and T_z span a four-dimensional space in the set of 3×3 traceless, symmetric tensors. Let $\overline{T}$ be the normal of the tensor field. We have the following theorem:

Theorem 4. *$\forall w,x,y,z \in \mathbb{R}$, let v_1, v_2, and v_3 be respectively the major, medium, and minor eigenvectors of a neutral tensor $t = wT_0 + xT_x + yT_y + zT_z$. Then $v_1^T \overline{T} v_1 = v_3^T \overline{T} v_3$.*

Theorem 4 indicates that given a neutral tensor in the linear tensor field $T(x,y,z)$, its unit major and minor eigenvectors must reside on the same level set of the quadratic function $v^T \overline{T} v$ on the unit sphere $\alpha^2 + \beta^2 + \gamma^2 = 1$ where $v = (\alpha, \beta, \gamma)$.

We now consider the following question: given a unit vector as the medium eigenvector, how many different ways can we find a unit major eigenvector and unit minor eigenvector, which must reside on the same level set of $v^T \overline{T} v$? The following results together address this question.

Theorem 5. *Given a medium eigenvector v_2 which resides on the k-th level set of $v^T \overline{T} v$, the corresponding major and minor eigenvectors must reside on the $-\frac{k}{2}$-th level set of $v^T \overline{T} v$.*

This implies that the number of solutions given the medium eigenvector v_2 is dependent on the number of intersection points of the plane whose normal is v_2 and the level set with the value $-\frac{v_2^T \overline{T} v_2}{2}$.

The following theorem characterizes the shape of these level sets.

Theorem 6. *Under structurally stable condition that $\overline{T}$ is non-degenerate, a level set of $v^T \overline{T} v$ on the unit sphere must be two non-intersecting non-circular spherical ellipses, except one situation where it is the union of two great circles, residing in two intersecting planes.*

Figure 4(a) illustrates this with an example. Note that while v_1, v_2, and v_3 are all unit vectors, we wish to parameterize the neutral surface of a 3D linear tensor field with as few parameters as possible. It turns out that we can use the medium eigenvectors to parameterize the neutral tensors with two singularities.

Given a unit medium eigenvector v_2, the plane P that passes though the origin whose normal is v_2 will intersect a typical level set $v^T \overline{T} v$ at four points, two per non-circular ellipse. Note that if v resides on one ellipse, $-v$ will reside on the other ellipse. Furthermore, if u and w are respectively the major and minor eigenvectors of a tensor, so are $-u$ and $-w$. Consequently, we only need to consider the intersection of the plane P with one ellipse. The two solutions u and w lead to two neutral

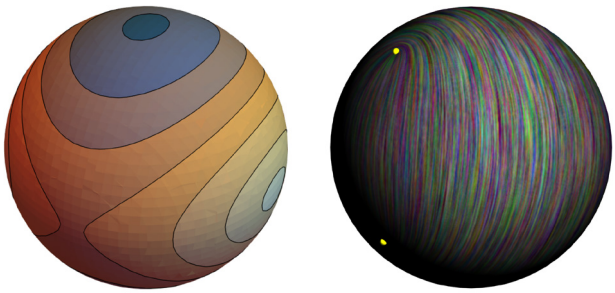

(a) (b)

Fig. 4: In (a): a level set of $v^T \overline{T} v$ on the unit sphere $\alpha^2+\beta^2+\gamma^2=1$ (where $v=(\alpha,\beta,\gamma)$) consists of two ellipses except in the degenerate case when it consists of two intersecting great circles (not shown in the example). In (b), the medium eigenvector manifold where the line field corresponds to one of the bisector fields between the major and minor eigenvector fields. The singularities (the yellow dots) correspond to the two degenerate cases in (a).

tensors, with opposite signs. However, only one of them can occur in the field due to Proposition 1. This means that for all but two planes whose normals are the medium eigenvectors, there is one corresponding neutral tensor in the tensor field. Thus, we can parameterize the neutral points in the field with the unit sphere modulo the inversive symmetry, except at two points. The following proposition makes this observation more rigourous.

Proposition 7. *Given a unit vector v, the tensor at (x,y,z) has v as its medium eigenvector if and only if*

$$M \begin{bmatrix} x \\ y \\ z \end{bmatrix} = -T_0 v \tag{20}$$

where M is the matrix $\begin{bmatrix} T_x v & T_y v & T_z v \end{bmatrix}$.

Let us consider a map from a neutral tensor t to a tangent line field on the unit sphere as follows (Figure 4(b)). We map the pair of antipodal points on the unit sphere corresponding to the medium eigenvector of t, i.e., $\pm v_2$. Then, the unit tangent directions at these points are defined as $\frac{v_1+v_3}{|v_1+v_3|}$, a bisector of the unit major eigenvector and the minor eigenvector of t. Note that this bisector is an eigenvector of the projection of $\overline{T}$ onto the plane orthogonal to v_2. This leads to a line field on the unit sphere (Figure 4(b)). Note that this line field has four wedges, corresponding to two pairs of antipodal points. In fact, each pair corresponds to the same singularity.

The two singularities correspond to the case when

$$v_1^T \overline{T} v_1 = v_3^T \overline{T} v_3 = b \tag{21}$$

where b is the medium eigenvalue of $\overline{T}$. In this case, the two planes normal to the given eigenvectors intersect the level sets at a circle, thus having infinitely many solutions for v_1 and v_3. In fact, these solutions can be parameterized by a circle with antipodal points identified. We refer to these two pairs of antipodal points as the singularities in the parameterization of the neutral surface. In addition, we refer to this sphere with two pairs of singularities, or, more precisely, an $\mathbb{RP}^2$ with two singularities, as the *medium eigenvector manifold*. For visualization purposes, we represent the medium eigenvector manifold as a sphere (Figure 4(b)) since $\mathbb{RP}^2$ is a non-orientable surface.

The following theorem shows that each singularity in the medium eigenvector manifold corresponds to a straight line in the domain of the tensor field.

Theorem 8. *Given a unit vector v where the projection of $\overline{T}$ onto the plane orthogonal to v is a degenerate two-dimensional tensor, the set of points on the neutral surface that have v as their medium eigenvector is a line.*

Figure 5 shows the neutral surfaces of two example tensor fields, each of which contains two straight lines (yellow) that correspond to the singularities of their respective medium eigenvector manifold.

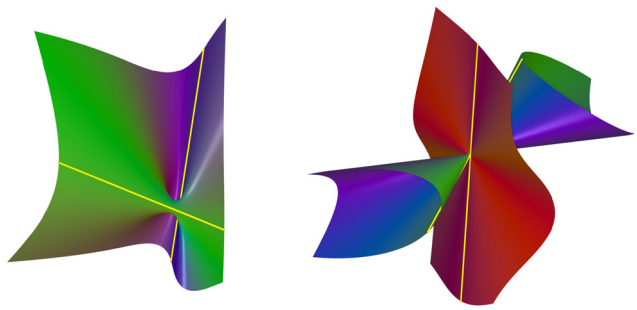

(a) (b)

Fig. 5: There are two configurations of neutral surfaces in a linear tensor field. In the first configuration (a) the handle is finite, while the second configuration (b) has the handle that connects at infinity. The singularities in the neutral surface are straight lines (yellow). The color encodes the medium eigenvectors and uses x, y and z components of the normalized medium eigenvectors as the *red*, *green* and *blue* components, respectively.

Topologically speaking, the neutral surface can be considered as the real projective space $\mathbb{RP}^2$ (sphere modulo antipodal identification) with two Möbius bands attached, one per the aforementioned singularity. Figure 6 illustrates the neighborhood of a singularity O (left) with some hyperstreamlines. Recall that the singularity is a topological circle in the medium eigenvector manifold. Consequently, lifting O onto a circle leads to a rectangular band (Figure 6 (b)) where O is a line segment (middle, red) so that the left side and right side are identified in reversed orientations. This leads to a Möbius band. Attaching two Möbius bands (one per singularity) to $\mathbb{RP}^2$ is equivalent to attaching a handle to $\mathbb{RP}^2$ [1].

Some extracted neutral surfaces are shown in Figure 5 where the handle is either finite (a) or infinite (b). Notice that when the handle is finite, the neutral surface intersects ∞ at one topological circle. In contrast, when the handle is infinite, the neutral surface intersects ∞ at two topological circles.

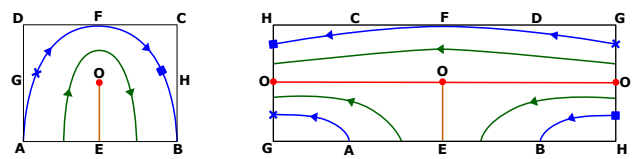

(a) (b)

Fig. 6: This figure illustrates the fact that the medium eigenvector manifold near a singularity can be modelled as attaching a Möbius band. Shown in (a) is a rectangular neighborhood of a singularity O (one of the yellow dots in Figure 4(b)) with some hyperstreamlines (colored curves). The singularity O corresponds to a topological circle. Consequently, the neighborhood can be better visualized as a rectangle (b) inside which the line corresponding to O is in the middle (red). The hyperstreamlines shown in (a) are also shown in (b) with the same colors. Note that the left side of the rectangle is identified with the right side of the rectangle in the reverse order in (b).

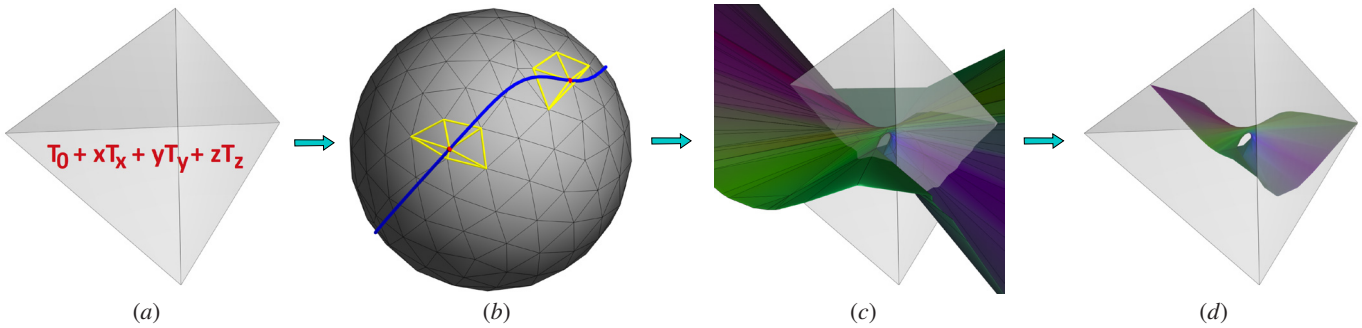

Fig. 7: From left to right, this figure illustrates our neutral surface extraction algorithm with an example tensor field. Starting from the input tensor field in a tetrahedron (a), we compute the corresponding medium eigenvector manifold which has two pairs of singularities (red dots). Also, the ∞ forms a loop ((b): blue). Next, we triangulate this manifold to ensure that the singularities are vertices of the triangle mesh (b). Due to the mapping between the medium eigenvector manifold and the neutral surface, we construct a triangulation of the neutral surface (c). Triangles totally outside the tetrahedron are discarded for efficiency. Finally, the neutral surface is clipped against the boundary of the tetrahedron, thus finding the neutral surface inside the tet.

5.2 Neutral Surface Extraction Algorithm

By using the parameterization defined in the previous section, we can generate the neutral surface at any given resolution. Given an input tensor field, we extract the neutral surface inside each tetrahedron in the mesh that tessellates the domain. The collection of the neutral surfaces inside the tetrahedra forms the neutral surface of the input tensor field. Next, we focus on finding the neutral surface of a linear tensor field inside each tetrahedron.

Given a linear tensor field $T(x,y,z) = T_0 + xT_x + yT_y + zT_z$ and a tetrahedron c (an example is shown in Figure 7(a)), our pipeline of extracting the neutral surface of $T(x,y,z)$ inside c is achieved as follows.

We start by triangulating the $\mathbb{RP}^2$ (half of the unit sphere) for the medium eigenvector (Figure 7(b)). This is achieved by considering the unit sphere as a round icosahedron and performing a number of Loop subdivisions to it. This guarantees the antipodal symmetry of $\mathbb{RP}^2$.

Next, we modify the mesh so that each singularity in the parameterization is also a vertex. This results in a triangulation of the medium eigenvector manifold (Figure 7(b)). We then find the x, y, z coordinates for each non-singularity vertex (Figure 7(c)) and connect three vertices in $\mathbb{R}^3$ as a triangle if their corresponding vertices form a triangle in the medium eigenvector manifold (Figure 7(b)).

Recall that a singularity in the parameterization corresponds to a line. Consequently, we extract the neutral surface around a singularity as follows (Figure 8). Given the 1-ring neighborhood of a singularity O (Figure 8 (a)), we convert O into a polygon (Figure 8 (b): red pentagon) whose number of sides matches the number of vertices adjacent to O. Each triangle in (a) is now a quad in (b) which can be split into two triangles by adding a diagonal. The corresponding neighborhood in $\mathbb{R}^3$ is shown in (c), which is a rectangular region bounded on the left and right by ∞. Since the singularity corresponds to a line, the parameterization is discontinuous and the limit approaching it from different directions gives different points. We use this to find the xyz coordinates of O_A, by calculating the limit of the parameterization as we approach the singularity((c): the red line in the middle) along the line OA. The detail of this step is given in Appendix B. The 3D locations of the O_B through O_E can be determined in a similar fashion.

Finally, we clip the triangle against the tetrahedron. For efficiency, we first cull all triangles that are entirely outside the tetrahedron. We then clip the remaining triangles against the faces of the tetrahedron in sequence. Each triangle that crosses the plane of a face is either split into a new triangle, or two quads that are then split into triangles. The intersection point of the neutral surface edge with the plane is determined by finding the point on the edge of the medium eigenvector manifold that maps to a point on this plane.

Note that the neutral surface intersects ∞ along a curve, which corresponds to a loop in the medium eigenvector manifold that goes through each singularity (Figure 7(b): blue loop). A triangle intersecting with the ∞ loop is invalid. However, after clipping any such triangle must lie entirely outside the tetrahedron and thus has been removed.

Observing that the neutral surface can be rather flat except near the handle, we wish to combine our technique with simpler techniques such as the A-patches method.

The A-patches method [11] is an iterative method that computes the zeroth level set of a given polynomial defined in a tetrahedron. The idea is to compute the Bernstein coefficients of the polynomial [11] and record them on a grid (Figure 9: the grid formed by colored dots). The A-patches method analyzes the signs of the coefficients (Figure 9: red for positive coefficients and blue for negative coefficients), which results in four scenarios. In the first, all coefficients are either all positive or all negative (Figure 9 (1a and 1b)). In this case, there is no zeroth level set in the tet. In the second and third scenarios, there is a single sheet (topological disk) of the zeroth level set, touching three faces (three-sided A-patch) or four faces (four-sided A-patch) of the tetrahedron, respectively (Figure 9 (2a and 2b)). In the likely case where the tests for these scenarios fail, the A-patches method will divide the tetrahedron into smaller tetrahedra, each of which will be again tested for A-patches. This process continues until either all tets (including the ones from subdivision) have all converged (no patch, a three-sided patch, or a four-sided patch), or the maximum number of iterations have been exceeded without convergence. Note that there is no guarantee the A-patches method will converge in finite iterations.

The difficulty with the A-patches method is that it assumes the surface is relatively flat and is mostly aligned with at least one face (three-sided A-patch) or one pair of opposing edges (four-sided A-patch) of the tetrahedron. This assumption breaks down where the surface has high curvature, such as the neutral surfaces near the handles (Figure 9 (3a and 3b)). This is where our method is more robust.

Consequently, we combine the strength of both methods. First, we perform the A-patches method without any subdivision. That is, if a tet fails the A-patches test, no subdivision is performed. Instead, for these tets we apply our parameterization-based neutral surface extraction method. This leads to more robust extraction of the neutral surfaces without incurring high computational cost and memory consumption with tetrahedral subdivision. Figure 1 (c-d) shows a comparison of the neutral surfaces extracted from our method (d) and from the pure A-patches method (c). Notice our method has fewer artifacts.

6 Performance

Measurements were taken on a computer with an Intel(R) Xeon(R) E3-1230 CPU running at 3.40GHz, 64GB of RAM, and an NVIDIA Quadro K420 GPU. The datasets that we used in this paper have a tetrahedral count on the order of 10^6. The running time for our degenerate curve extraction method is between 0.5 and 1 seconds. This represents

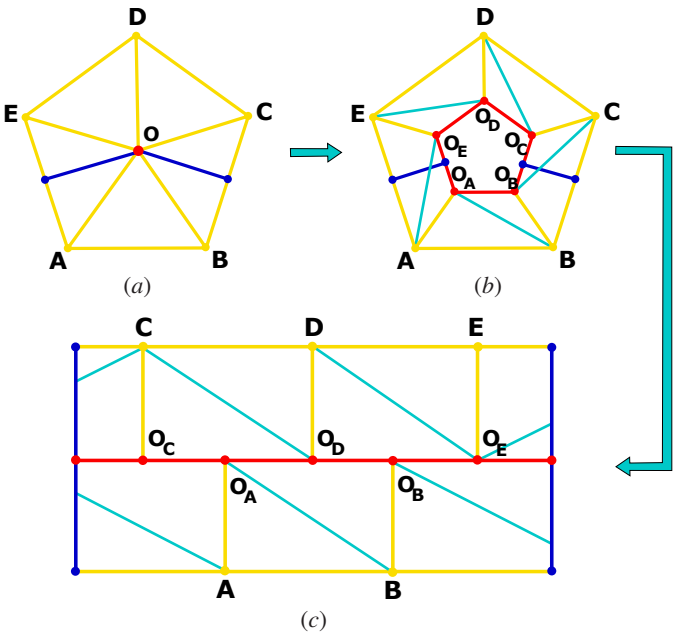

Fig. 8: This figure illustrates the extraction of neutral surfaces around a singularity in the parameterization. In (a) we show the 1-ring neighborhood of a singularity O in the medium eigenvector manifold where the line of ∞ (blue) passes through O. The singularity corresponds to a topological circle in the neutral surface. Consequently, for triangulation purposes we expand O into a polygon ((b): the red pentagon) whose number of sides matches the number of vertices adjacent to O. This turns each triangle in the original triangulation (a: yellow triangles) into a quad in (b). We split each quad into two triangles. The corresponding neighborhood in $\mathbb{R}^3$ is shown in (c). Note that since this is a Möbius band, the left and right sides of the rectangle are connected in reverse like in Figure 6. Also notice that the vertices on either side of the singularity line do not match up, thus producing T-junctions. This is a limitation of our extraction method.

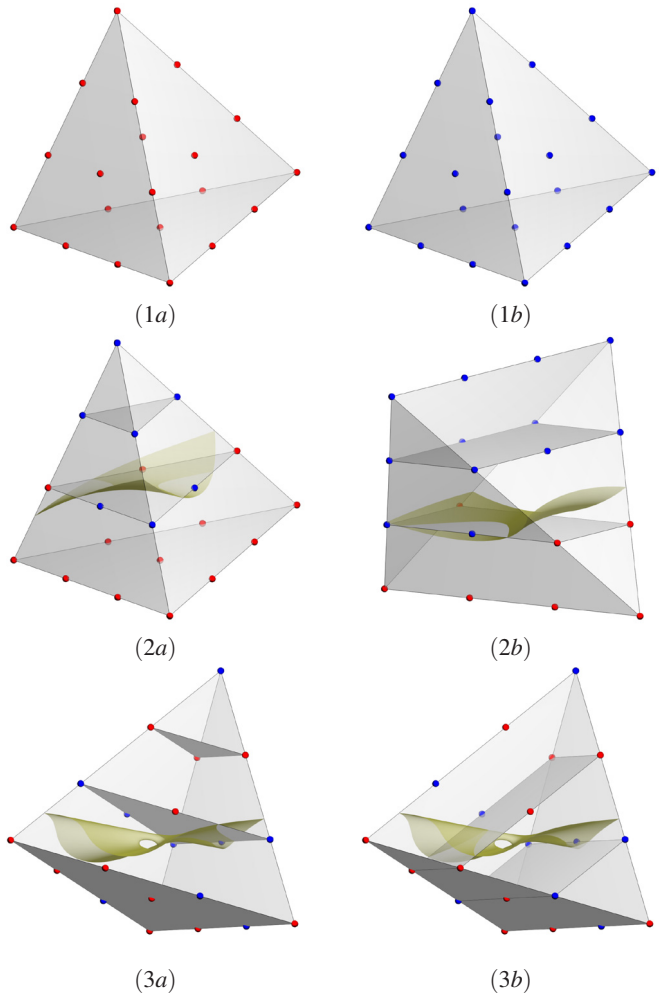

Fig. 9: This figure shows the cases of the A-patches method [11]. The signs of the coefficients are color coded at each grid point: red for positive and blue for negative. If they are all the same sign (1a and 1b), then there is no zeroth level inside the tetrahedron. If a layer exists that separates the grid into two sides such that the coefficients on one side are all positive (red) and on the other side all negative (blue), then there is one sheet of the zeroth level set that either intersects three faces (three-sided A-patch) (2a) or four faces (four-sided A-patch) (2b) of the tet. When no such separation layer exists (cases 3a and 3b), then the tet is subdivided recursively.

an order of magnitude of speed gain over the method of Palacios et al. [13]. For extracting neutral surfaces, the running time of our method is between 1 and 10 seconds. On average, the time to extract neutral surfaces using our method is about 67% of the time using the A-patches method [13].

7 Applications

The engineering community has high interest in structural deformation for research in areas such as material science, astrophysics and geoscience where novel materials, rocks, and soil are subject to some kind of pressure. In medical research, the stress analysis of an implant inside bones is needed [5]. Despite such a wide range of applications, a scalar representation of this stress tensor is predominantly used due to the lack of visualization tools to extract meaningful knowledge from the stress tensor fields. Our topology-driven visualization system extracts and visualizes important topological features of such stress tensors which can help in improving fundamental understanding of tensor fields.

Figure 10 shows a torus (representing a tire) that has boundary conditions at the top and the bottom. When a tire is pressed to the ground during rolling, the top side of the tire is indirectly constrained due to the axle that connects the tire to the car, and the bottom side of the tire is displaced by the ground. Here, we investigate the topology in stress tensors when the torus is fixed at the top over a line region and is displaced at the bottom side with another line region that is symmetrically placed as shown in Figure 10(a). Due to the required flexibility in joining the axles to the tires, sometimes there is a camber that allows the tire to be tilted. We shorten the line region on the top by half as shown in Figure 10(b) to approximate this real life situation.

We name the symmetric boundary case, symmetric-boundary; and the other case, camber-boundary. In Figure 11 ((a) and (e)), we compare the degenerate curves detected for these two cases. Note that the camber-boundary results in Figure 11(e) clearly indicate the asymmetry in loading. In Figure 11 ((b) and (f)), we compare the corresponding neutral surfaces. There is a continuous neutral surface on the outer contour of the torus in Figure 11(f) while there are 4 disjoint groups of neutral surfaces in Figure 11(b) due to the symmetric-boundary. The camber-boundary allows a larger free region on the top side and enables continuous propagation of stress. This difference in the neutral surfaces reflects the difference in the loading.

In addition to boundary conditions, engineers focus on material description. In Figure 11 ((a) and (c)), we contrast the degenerate curves for the same torus with different material compressibility levels for the symmetric-boundary case. The material in Figure 11(a) is highly incompressible rubber-polymer while the material in Figure 11(c) is compressible for some special construction polymer. Notice that the degenerate curves on the left and right are aligned with the torus. In

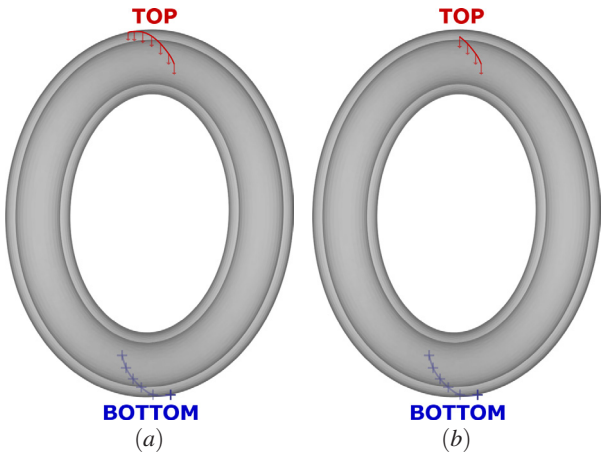

Fig. 10: A symbolic structure of a tire standing on the ground. From the weight of the vehicle this tire supports, the top portion of the torus comes downward. A line segment at the top of the torus moves downward in (a) when a concentrated force (shown with red arrows pointing downwards) is applied to it. Only half of the line segment used in (b) moves as shown with red arrows pointing downwards. The contact with the ground (shown as blue cross symbols at the bottom of (a) and (b)) is fixed in space through a line segment that symmetrically mirrors the segment on top in (a).

contrast, some degenerate curves ((c): green degenerate curves on the left and right side) run perpendicularly to the torus's shape, indicating undesirable behavior due to the compressible nature of the material. The corresponding neutral surfaces are shown in Figures 11 ((b) and (d)). The incompressible material in Figure 11(b) creates a higher amount of shear deformation and this leads to a larger area of neutral surface than that in Figure 11(d). Such a difference is extremely difficult to measure in engineering practices for rubber polymers that have different chemical and physical constructions. These neutral surfaces can potentially be a feasible device to differentiate materials in terms of their deformation behavior.

Figure 1(d) is an angled view of the bottom right quadrant of the neutral surface of the compressible torus volume used in Figure 11(d). In Figure 1(c), the same neutral surface is extracted with the method of Palacios et al. [13]. Our method captures the neutral surface more completely, including features that the method of Palacios et al. missed, such as the thin features on the lower-left corner. With more accurate extraction of neutral surfaces, we can better interpret the physics behind the simulations of real life phenomena. This is the benefit of our new extraction method; otherwise, with broken surfaces, the interpretation can be erroneous.

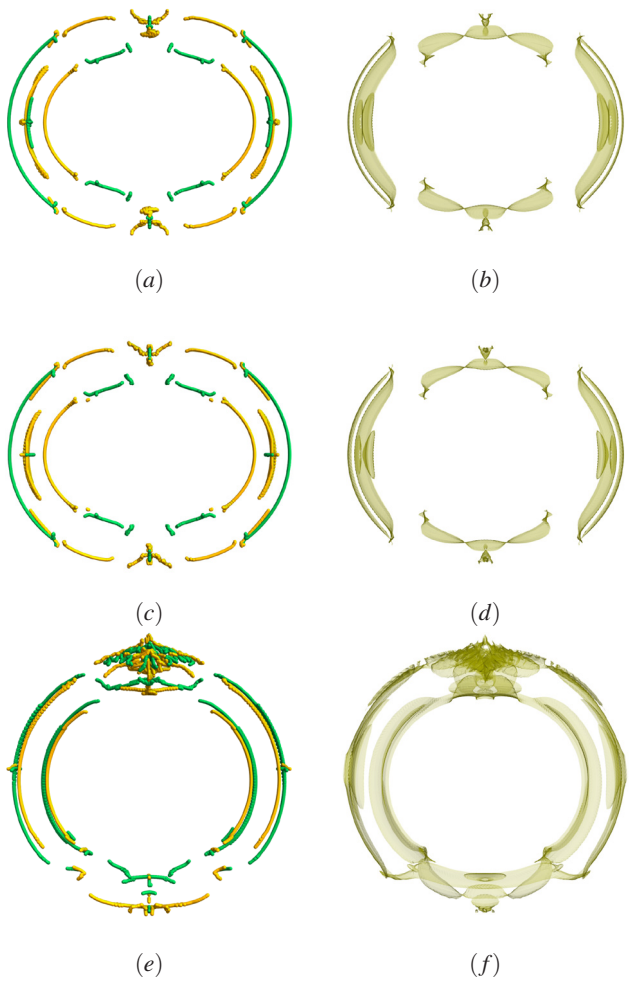

Fig. 11: Side view of degenerate curves and neutral surfaces for the symmetric-boundary (a-d) and the camber-boundary cases (e-f). The distribution of the degenerate curves is symmetric reflecting the symmetric boundary condition in (a) and (c). Symmetric segments of the neutral surfaces in (b) and (d) also reflect the boundary conditions. The degenerate curves and neutral surfaces for the camber-boundary case are shown in (e) and (f) respectively. The material used in (a), (b), (e), and (f) is highly incompressible, and is highly compressible in (c) and (d).

8 Conclusion and Future Work

In this paper we have developed novel topological analysis of the degenerate curves and neutral surfaces of 3D symmetric tensor fields, which leads to a parameterization respectively for degenerate curves and neutral surfaces and consequently more robust and faster extraction methods.

Our technique is not without limitations. For example, our methods assume structurally stable conditions. That is, degenerate points form curves and neutral points form surfaces. While we have not observed a problem with this assumption in practice, it would be desirable to extend our analysis to handle other theoretically possible scenarios such as when degenerate points form surfaces and volumes while neutral points form curves and volumes. Also, the sampling rate of the degenerate curve and neutral surface parameterizations breaks down when there is nearly a bifurcation, a place where the degenerate curve or neutral surface is not a manifold. Another limitation of our neutral surface extraction method is that it still makes use of the A-patches methods, a relatively expensive process. In the future, we wish to explore faster techniques.

In the future, we plan to extend our research to 3D asymmetric tensor fields as well as time-varying tensor fields. In addition, the analysis that we have developed can find use in applications in geometry processing. We plan to leverage on discoveries in this field.

Acknowledgments

We wish to thank our anonymous reviewers for their valuable feedback and suggestions. Jonathan Palacios and Ritesh Sharma have contributed to the linear tensor field design and visualization program that has been helpful to the research. This research is partially supported by NSF awards (# 1566236) and (# 1619383).

References

[1] M. Armstrong. *Basic Topology*. Undergraduate Texts in Mathematics. Springer, 1990.

[2] L. Cammoun, C. A. Castano-Moraga, E. Munoz-Moreno, D. Sosa-Cabrera, B. Acar, M. Rodriguez-Florido, A. Brun, H. Knutsson, J. Thiran, S. Aja-Fernandez, R. de Luis Garcia, D. Tao, and X. Li. *Tensors in Image Pro-*

cessing and Computer Vision. Advances in Pattern Recognition. Springer London, London, 2009.

[3] J. Damon. Generic structure of two-dimensional images under gaussian blurring. *SIAM Journal on Applied Mathematics*, 59(1):97–138, 1998.

[4] T. Delmarcelle and L. Hesselink. Visualizing second-order tensor fields with hyperstream lines. *IEEE Computer Graphics and Applications*, 13(4):25–33, July 1993.

[5] C. Dick, J. Georgii, R. Burgkart, and R. Westermann. Stress tensor field visualization for implant planning in orthopedics. *IEEE Transactions on Visualization and Computer Graphics*, 15(6):1399–1406, 2009.

[6] W. Fulton. *Algebraic Curves*. Mathematics Lecture Note Series. W.A. Benjamin, 1974.

[7] J. Greene. "traces of matrix products. *Electronic Journal of Linear Algebra.*, 27, 2018. doi: 10.13001/1081-3810.1999

[8] G. Guennebaud, B. Jacob, et al. Eigen v3. http://eigen.tuxfamily.org, 2010.

[9] L. Hesselink, Y. Levy, and Y. Lavin. The topology of symmetric, second-order 3D tensor fields. *IEEE Transactions on Visualization and Computer Graphics*, 3(1):1–11, Mar. 1997.

[10] A. Kratz, C. Auer, M. Stommel, and I. Hotz. Visualization and analysis of second-order tensors: Moving beyond the symmetric positive-definite case. *Computer Graphics Forum*, 32(1):49–74, 2013. doi: 10.1111/j.1467-8659.2012.03231.x

[11] C. Luk and S. Mann. Tessellating algebraic curves and surfaces using a-patches. In *GRAPP*, pp. 82–89, 2009.

[12] J. Palacios, L. Roy, P. Kumar, C. Hsu, W. Chen, C. Ma, L. Wei, and E. Zhang. Tensor field design in volumes. *ACM Trans. Graph.*, 36(6):188:1–188:15, 2017. doi: 10.1145/3130800.3130844

[13] J. Palacios, H. Yeh, W. Wang, Y. Zhang, R. S. Laramee, R. Sharma, T. Schultz, and E. Zhang. Feature surfaces in symmetric tensor fields based on eigenvalue manifold. *IEEE Transactions on Visualization and Computer Graphics*, 22(3):1248–1260, Mar. 2016. doi: 10.1109/TVCG.2015.2484343

[14] J. Richter-Gebert. *Perspectives on Projective Geometry: A Guided Tour Through Real and Complex Geometry*. Springer Berlin Heidelberg, 2011.

[15] L. E. Spence, A. J. Insel, and S. H. Friedberg. *Elementary linear algebra*. Prentice Hall, 2000.

[16] G. Strang. *Introduction to Linear Algebra*. Wellesley-Cambridge Press, Wellesley, MA, fourth ed., 2009.

[17] X. Tricoche, G. Kindlmann, and C.-F. Westin. Invariant crease lines for topological and structural analysis of tensor fields. *IEEE Transactions on Visualization and Computer Graphics*, 14(6):1627–1634, 2008. doi: 10.1109/TVCG.2008.148

[18] X. Tricoche, G. Scheuermann, and H. Hagen. A Topology Simplification Method For 2D Vector Fields. In *Proceedings IEEE Visualization 2000*, 2000.

[19] E. Zhang, J. Hays, and G. Turk. Interactive tensor field design and visualization on surfaces. *IEEE Transactions on Visualization and Computer Graphics*, 13(1):94–107, 2007.

[20] Y. Zhang, J. Palacios, and E. Zhang. Topology of 3d linear symmetric tensor fields. In I. Hotz and T. Schultz, eds., *Visualization and Processing of Higher Order Descriptors for Multi-Valued Data*, pp. 73–91. Springer International Publishing, Cham, 2015.

[21] X. Zheng and A. Pang. Topological lines in 3d tensor fields. In *Proceedings IEEE Visualization 2004*, VIS '04, pp. 313–320. IEEE Computer Society, Washington, DC, USA, 2004. doi: 10.1109/VISUAL.2004.105

[22] X. Zheng, B. Parlett, and A. Pang. Topological structures of 3D tensor fields. In *Proceedings IEEE Visualization 2005*, pp. 551–558, 2005.

[23] X. Zheng, B. N. Parlett, and A. Pang. Topological lines in 3d tensor fields and discriminant hessian factorization. *IEEE Transactions on Visualization and Computer Graphics*, 11(4):395–407, July 2005.

[24] V. Zobel and G. Scheuermann. Extremal curves and surfaces in symmetric tensor fields. *The Visual Computer*, Oct 2017. doi: 10.1007/s00371-017-1450-1